

Sub-meter wind detection with pulsed coherent Doppler lidarYunpeng Zhang ¹, Jinlong Yuan,² Yunbin Wu,¹ Jingjing Dong ² and Haiyun Xia^{1,2,3,4,*}¹*School of Earth and Space Sciences, University of Science and Technology of China, Hefei 230026, China*²*School of Atmospheric Physics, Nanjing University of Information Science and Technology, Nanjing 210044, China*³*Hefei National Laboratory for Physical Sciences at the Microscale, USTC, Hefei 230026, China*⁴*Institute of Software, Chinese Academy of Sciences, Beijing 100190, China*

(Received 20 September 2022; accepted 16 February 2023; published 27 February 2023)

High-resolution wind detection plays a crucial role in aviation safety and aerodynamic research. A pulsed coherent Doppler wind lidar (CDWL) with sub-meter/sub-second resolution is demonstrated. The pseudorandom modulation (PRM) method is used to break the link between laser pulse duration and spatial resolution. Benefiting from the flexible pulse duration, the detection accuracy degradation related to the short pulse is largely mitigated. The backscattered spectra and wind profiles measured by the proposed lidar are compared with those obtained by a conventional pulsed CDWL, validating its capacity of radial wind detection within 700 m at 0.9 m/0.5 s resolution. With the help of the proposed high-resolution lidar, the meter-scale perturbation on the wind field from an electric fan is detected in a field experiment.

DOI: [10.1103/PhysRevFluids.8.L022701](https://doi.org/10.1103/PhysRevFluids.8.L022701)

Introduction. The meter-scale complex flow, such as turbulence, has long been a research hotspot. The field measurement is indispensable in the fluid study. In areas like aviation safety and aerodynamics, high-resolution wind detection is required [1,2]. For example, the aircraft wake turbulence is regarded as one of the most dangerous hazards in aviation, which may make the aircraft run out of control, especially during the departing and landing process [3]. Through precise measurement of aircraft wake vortex and atmospheric conditions, the flight safety and aircraft aerodynamic efficiency can be largely improved [4]. In addition, the remote sensing of fine wind fields is of great value to wind energy applications and atmosphere researches [5–7]. Turbulence flow is always three-dimensional and unsteady with a large range of motions, thus the resolution of measurements must be fine enough to capture the small-scale dynamic process (the Kolmogorov microscale). It's urgently needed to develop effective detection tools to observe meter-scale flows for further revealing their mechanism.

As a fast-developing remote sensing technique, the coherent Doppler wind lidar (CDWL) is a promising candidate for high-resolution wind detection. Owing to its advantages on accuracy, robustness, and background light tolerance [8], the CDWLs are widely employed in many areas. Through the deep analysis of the backscattered spectrum, applications like cloud phase identification [9], turbulence analysis [10], and air pollution detection [11] can be supported.

In general, the CDWL can be divided into two categories: continuous-wave (CW) and pulsed. Typically, the CW lidar can achieve a high spatial resolution (SR) within a small range [12,13], but lacks the capacity of wide-range wind profiling. Meanwhile, the pulsed CDWL has advantages in long-distance and wide-range measurement [8], which meets the requirement of aircraft wake

*hsia@ustc.edu.cn

vortex detection. Up to now, numerous efforts have been spent to enhance the pulsed CDWL's SR to meter scale. Multistage amplification [14] and pulse coding technique [15] are used to increase the transmitted power under a short pulse duration, achieving the SR of 3 m and 6 m, respectively. To further mitigate the accuracy degradation caused by the wide spectrum of a short pulse, the differential correlation pair (DCP) [16,17], and pseudorandom modulation (PRM) technique [18,19] are proposed to improve the SR without shortening the pulse duration. In the DCP method, as the common parts in the paired pulses are eliminated in the difference operation, the SR of 3 m is achieved [17]. Meanwhile, in the PRM method, by linking the SR with the modulation rate, the SR can be improved to 1.8 m [19]. However, to enhance the SR to sub-meter scale, the system design needs to be more elaborate. At such a high SR, the amplified spontaneous emission (ASE) should be further isolated from the faint backscattered signal. The balance between saturation and magnification in a high sensitivity photodetector also needs to be reconsidered.

Here, we propose a high-resolution CDWL based on the PRM technique. By optimizing the system layout and hardware parameters, the spatial/temporal resolution of the pulsed CDWL is promoted to sub-meter/sub-second scale. This paper is organized as follows. The principle and system characteristics of the PRM lidar are described in Sec. II. To validate the performance of the proposed lidar, the comparative experiment with a conventional pulsed CDWL and the detection of the artificial perturbation on wind field are conducted. The high-resolution wind detection results are presented in Sec. III. Finally, the performance and prospect of the high-resolution CDWL are summarized in Sec. IV.

Experiment setup. a. Principle. In the original design of the PRM method, the phase modulation is considered to have a rectangular shape. However, under a limited bandwidth, the rising and falling edges of the modulating signals have to be taken into consideration, especially at high modulation rate. To solve this problem, the mapping between the pseudorandom binary sequence (PRBS) and phase shift states can be used [19]. Let $g(t)$ denote the baseband transition function of the phase modulation and $b[m]$ denote the unipolar PRBS. The pseudo-random modulating signal can be expressed as

$$B(t) = \exp \left[j\pi \sum_m b[m]g(t - mT) \right]. \quad (1)$$

After modulation, the transmitted signal is

$$E(t) = A(t) \exp(j2\pi f_c t) \cdot B(t), \quad (2)$$

where $A(t)$ is the amplitude envelope of pulses, and f_c is the carrier frequency.

In demodulation, the received signal would be demodulated by the complex conjugation of the delayed modulating signal $B^*(t - t_0)$ to extract the backscattered signal from distance $z_0 = ct_0/2$:

$$r_{de}(t, t_0) = r(t) \cdot B^*(t - t_0), \quad (3)$$

where $r(t)$ is the atmospheric backscattered signal after heterodyne detection. As $B(t)B^*(t) = 1$, the negative impact of the noninstantaneous transition under limited bandwidth can be avoided.

b. System configuration. The layout of the proposed high-resolution CDWL is shown in Fig. 1. In the seed module, a continuous-wave laser is split into two parts with the major and minor part serving as the source of the transmitted signal and the local oscillator (LO), respectively. The continuous wave is chopped into pulses at 10 kHz by the built-in acousto-optic modulator (AOM) of the seed laser. The pseudorandom phase modulation is applied on the pulses by an electro-optic phase modulator (EOPM), where the modulating signal is generated from a 14 bit M sequence based on Eq. (1). In the amplifier, two erbium-doped fiber amplifiers (EDFA) are used as the prestage and powerstage to raise the laser's average power to 1 W, corresponding to the pulse energy of 100 μ J. A second AOM is inserted between the two EDFAs to suppress the impact of the ASE noise. The total frequency shift introduced by the AOMs is 160 MHz.

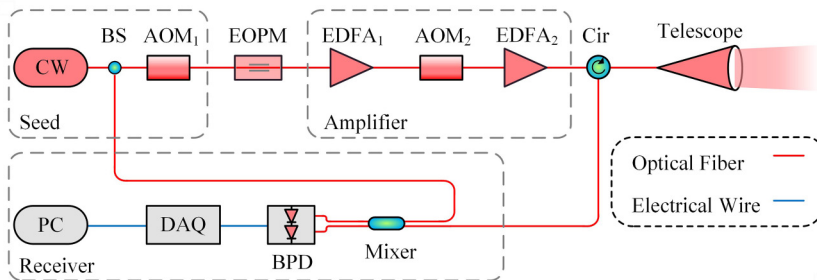


FIG. 1. System layout of the high-resolution lidar. CW, continuous-wave laser; BS, beam splitter; Cir, circulator; and PC, personal computer.

After being received by a 100-mm telescope, the backscattered optical signal is mixed with the LO and then beating on a balanced photodetector (BPD). The optical signal would be down converted into an analog electrical signal in intermediate frequency (IF) band. Then, the analog signal is continuously digitalized at 1 GSps by a home-made data acquisition system (DAQ) and demodulated in a computer. Typically, the wind velocity estimation accuracy can be improved by incoherently accumulating the backscattered spectra over time [20]. Here, the averaging time is set to be 0.5 s. For each spectrum, the sequence length in the discrete Fourier transform is extended to 8192 through zero padding, leading to the frequency interval of 0.122 MHz.

c. Instrument characterization. In the transmitter, the bit interval of the phase modulation is configured as 6 ns to realize the SR of 0.9 m. The modulated lightwave is shown in Fig. 2(a) by an eye diagram, while the enlarged view is shown in Fig. 2(b). In the eye diagram, the time jitter of the cross point is less than 0.5 ns. Besides, the intensity envelope of the pulses is also plotted in Fig. 2(a). It's noted that the modulated pulses share the same intensity envelope as the intensity would not be changed in the phase modulation. The full width at half maximum (FWHM) of the intensity envelope is measured as 402 ns, leading to the laser peak power of 250 W. Benefiting from the pseudorandom phase modulation and the large core diameter of the EDFA's output fiber, the waveform wouldn't be distorted by the stimulated Brillouin scattering (SBS) even at such a high power [21,22].

In the receiver, the noise is mainly from the additive noise of the BPD. To balance the impact of the shot noise and the saturation of the detector, the power of the LO is optimized to 1 mW. Figure 2(c) shows the noise spectra of the BPD measured by a spectrum analyzer with the resolution bandwidth (RBW) of 100 kHz. By comparing the noise power at the LO open and close, the excess noise factor [23] of the receiver can be obtained as 1.920.

Results. a. Comparison with conventional pulsed CDWL. First, to validate the performance of the proposed CDWL, the measurement results of the proposed high-resolution lidar are compared with a conventional pulsed (CP) CDWL. The SR of the CP lidar is about 60 m, roughly estimated by the

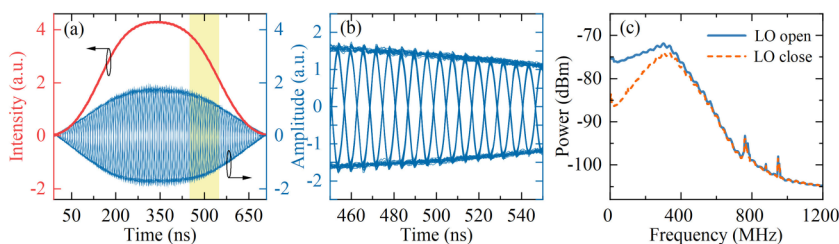


FIG. 2. (a) Eye diagram and intensity envelope of the modulated lightwave in the PRM method. (b) Enlarged eye diagram of the modulated lightwave. (c) Noise spectrum of the balanced photodetector.

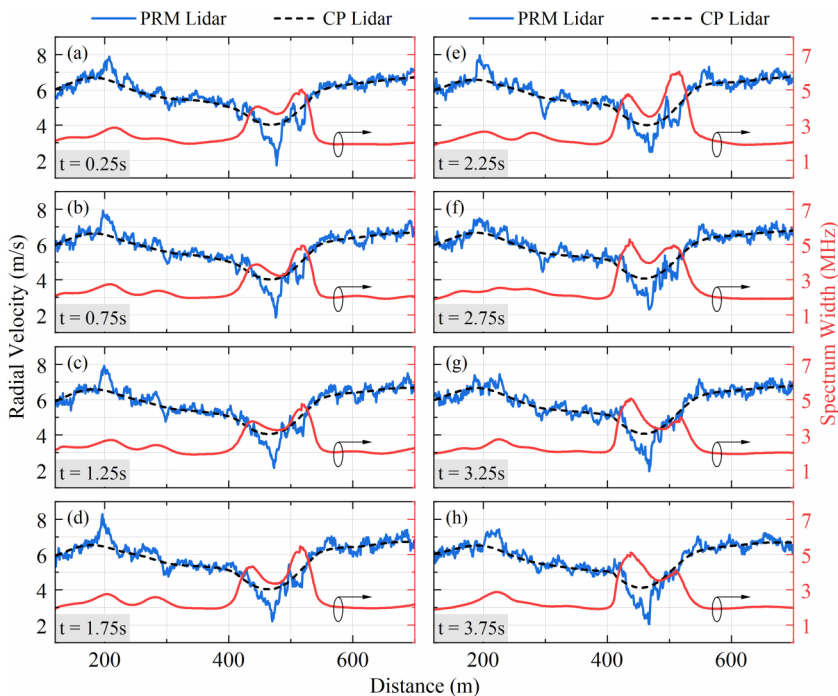


FIG. 3. (a)–(h) Continuous measurement results in four seconds. Left axis: radial wind velocity profiles of the two lidars; right axis: spectrum width of the CP lidar.

FWHM pulse duration [20]. The radial wind velocity is derived from the Doppler frequency shift, which is obtained by the Gaussian fit in both lidars. In continuous wind detection of 4 s, the wind profiles are plotted in Fig. 3 with respect to the left axis.

As indicated by the blue solid line and the black dashed line in Fig. 3, the wind velocity profiles obtained by the two methods show similar trends during the measurement. More details can be observed in the high-resolution wind profiles of the proposed lidar. For instance, differences between the two sets of profiles exist at distances like 200 m and 480 m. Due to the low SR of the CP lidar, the large gradient in the wind field is wiped out. As described in Ref. [24], when wind shear exists in one SR cell, the backscattered spectrum would be broadened. The FWHM spectrum width of the CP lidar is indicated by the right axis of Fig. 3. At the distances where the differences between the two sets of profiles occur, the spectrum widths of the CP lidar increase evidently, which verifies the wind shear detected by the proposed lidar.

Figure 4 shows the backscattered spectra at 350 m and 480 m. For clarity, the spectra curves at different time are shifted in the y axis. In Figs. 4(a) and 4(b), the spectra measured by the proposed lidar show a smooth trend through time. The continuity further implies the reliability of the measurement results to a certain extent. As a comparison, the spectra of the CP lidar are shown in Figs. 4(c) and 4(d). In Fig. 4(d), the spectrum broadening effect can be observed clearly. In contrast, the spectrum widths in Fig. 4(c) are close to those in Fig. 4(a) at 350 m, where the retrieved velocities obtained by the two lidars are similar. Incidentally, the signal power of the CP lidar is higher, as the signal diversity equivalently increased with the lower SR [20].

b. Detection of perturbation on wind field. With the help of the high-resolution CDWL, the detection of wind field perturbation from an electric fan is attempted. As illustrated in Fig. 5, the lidar and an electric fan with diameter of 0.75 m are placed on the ninth floor of the laboratory building (QiXiang Building) and the roof of another building (ShangXian Building), respectively.

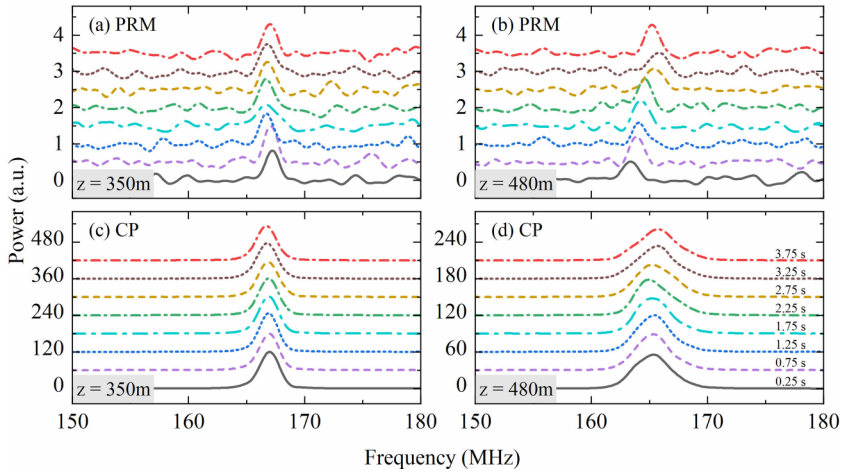


FIG. 4. Backscattered spectra at 350 m and 480 m measured by the (a), (b) PRM and (c), (d) CP lidars continuously.

The heights of the telescope and the fan are almost the same, and their horizontal distance is about 329 m.

Figure 6(a) shows the radial wind velocity profile measured in 4 s. A narrow ribbon structure (in the red dashed square) can be observed around 329 m, corresponding to the perturbation of the fan. The zoomed wind profiles around the perturbation are continuously plotted in Figs. 6(c) to 6(j). As the air flow generated by the fan is to the opposite direction of the atmospheric background wind field, the magnitude of the wind velocity drops near the fan, i.e., the wind velocity changes from negative to near zero. Besides 329 m, other ribbon structures also exist in Fig. 6(a), like around 175 m and 220 m, which can be attributed to the natural wind shear. When calculating the shear intensity of the wind field in radial direction [24], the mean shear intensity around 329 m can be as high as 1.5 s^{-1} . Meanwhile, the shear intensity at other distances would not exceed 0.5 s^{-1} , as illustrated in Fig. 6(b).

The atmospheric backscattered spectra around the fan are illustrated in Fig. 7, where the y axis shifts are used for clarity. Compared with other curves, the blue solid line marked as 328.7 m has the most obvious central frequency shift, which is consistent with the distance between the lidar and the fan. If taking the spectrum at 326.9 m (black dashed line) as a reference, a slight spectrum broadening effect can be observed in other spectra closer to the fan. As the diameter of the fan is



FIG. 5. Illustration of the experiment location and instruments layout.

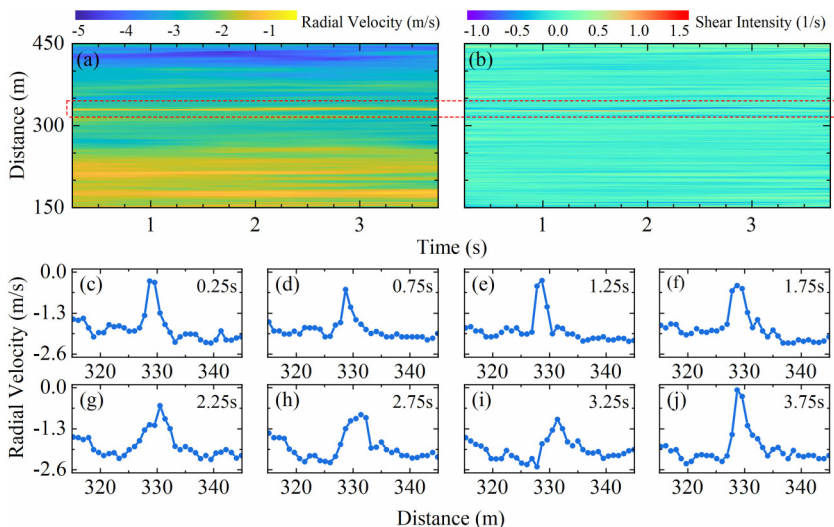


FIG. 6. (a) Continuous radial wind profiles in 4 s with spatial/temporal resolution of 0.9 m/0.5 s. (b) Radial shear intensity of the wind field. (c)–(j) Zoomed wind profiles between 315 m and 345 m, where the perturbation from the fan occurs around 329 m.

only 0.75 m, the broadening suggests that the wind field perturbation from the fan still has finer structures with the scale of less than 0.9 m.

To demonstrate the reliability of observation, the narrowband carrier-to-noise ratio (CNR_n) [20] and the derived Cramer-Rao lower bound (CRLB) [25] in the measurement are calculated. Admittedly, the real uncertainties of the measurement may be higher than the CRLB, it can still provide a preliminary estimation of the accuracy. As shown in Fig. 8(a), there is a drop of the CNR_n around 329 m, which could be attributed to the influence of the small-scale turbulence introduced by the fan.

To further reveal the structure of the wind field, the radial wind velocity in Fig. 6(a) is used for turbulent energy spectrum analysis. According to the locally isotropic turbulent hypotheses of

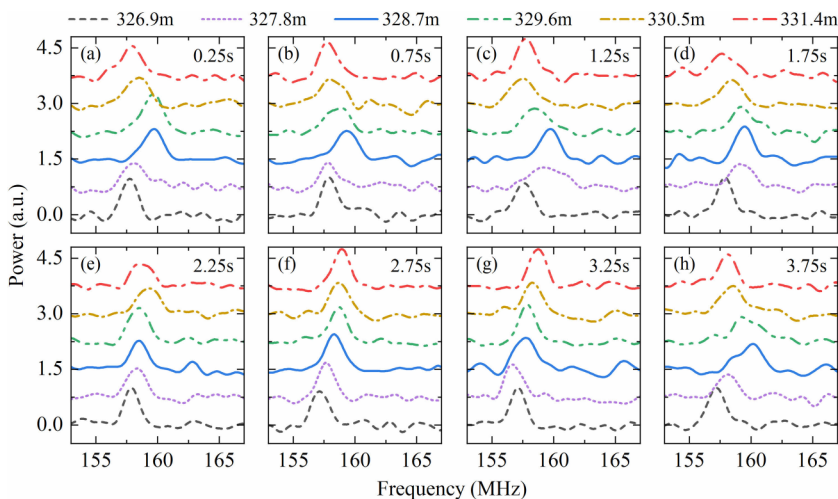


FIG. 7. (a)–(h) Backscattered spectra around the fan continuously measured in four seconds.

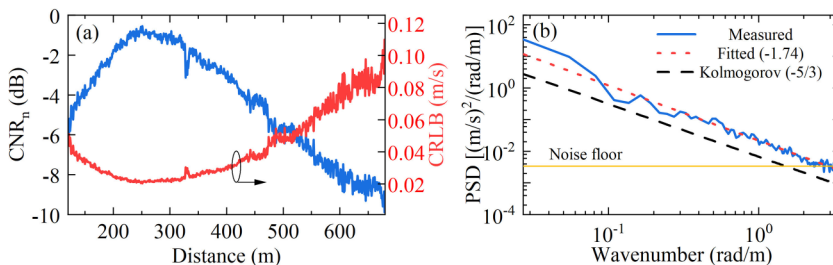


FIG. 8. (a) Narrowband CNR and corresponding CRLB. (b) Spectrum of the observed wind field, where the noise floor is around $3.9 \times 10^{-3} (\text{m s}^{-1})^2/(\text{rad m}^{-1})$.

Kolmogorov, the observed turbulent spectrum of the radial velocity obeys the $-5/3$ power law in the inertial subrange, specifically

$$\Phi_1(\kappa) = C_\kappa \langle \epsilon \rangle^{2/3} \kappa^{-5/3}, \quad (4)$$

where $\Phi_1(\kappa)$ is the one-dimensional longitudinal spectral density, κ is the wavenumber, $\langle \epsilon \rangle$ is the mean value of the energy dissipation rate, and the C_κ is the Kolmogorov constant which can be presumed as 0.53 [26]. It's noted that κ is defined as $\kappa = 2\pi/\lambda$ here, with λ being the wavelength of the atmospheric fluctuation. The measured power spectral density (PSD) averaged over 4 s is shown in Fig. 8(b). The fitted power law index of the curve is -1.74 , and a flattening of the spectrum at $\kappa > 2.1 \text{ rad m}^{-1}$ can be observed. This suggests that the observation of the $-5/3$ power law down to the length scale of 3 m ($2\pi/2.1$) is realized. The noise floor in Fig. 8(b) is around $3.9 \times 10^{-3} (\text{m s}^{-1})^2/(\text{rad m}^{-1})$. By integrating the noise floor on the wavenumber, the root mean square (RMS) value of the velocity noise in the measurement is calculated as 0.12 m/s. Moreover, the mean energy dissipation rate can be retrieved from Fig. 8(b) and Eq. (4) as $\langle \epsilon \rangle \approx 7.4 \times 10^{-3} \text{ m}^2 \text{ s}^{-3}$, which is close to the typical value observed at the bottom of the atmospheric boundary layer [24].

Conclusion. A high-resolution pulsed CDWL utilizing pseudorandom phase modulation is demonstrated. Through decoupling the spatial resolution and the pulse duration, the pulse energy constraint raised by the limited laser peak power is released. At laser peak power of 250 W, the pulse energy is amplified to up to 100 μJ . Meanwhile, the wide spectrum resulting from the short duration is avoided. In experiments, continuous radial wind profile measurement within 700 m is demonstrated at spatial/temporal resolution of 0.9 m/0.5 s. The measurement results of the proposed high-resolution lidar are compared with those of a conventional low-resolution CDWL. During the measurement, high-resolution wind shear detection is realized, and the results are verified by the spectrum width changes of the conventional CDWL. Moreover, the meter-scale perturbation on the wind field from an electric fan is detected.

By upgrading the laser power, the temporal resolution could be improved to 0.1 s. Considering the huge amount of the digitized raw data, real-time processing is the main obstacle to be overcome before promoting the application of the proposed system. As the high-speed lidar signal processing has already been achieved by an FPGA [27], we believe the real-time high-resolution wind detection with the proposed CDWL could be implemented in the near future. Besides, to further demonstrate the accuracy of the high-resolution CDWL, a comparative experiment with the *in situ* anemometer in a wind tunnel is under preparation.

[1] L. Thobois, J. P. Cariou, and I. Gultepe, Review of lidar-based applications for aviation weather, *Pure Appl. Geophys.* **176**, 1959 (2019).

- [2] T. J. Larsen, H. A. Madsen, G. C. Larsen, and K. S. Hansen, Validation of the dynamic wake meander model for loads and power production in the Egmond aan Zee wind farm, *Wind Energy* **16**, 605 (2013).
- [3] J. Li, C. Shen, H. Gao, P. W. Chan, K. K. Hon, and X. Wang, Path integration (pi) method for the parameter-retrieval of aircraft wake vortex by lidar, *Opt. Express* **28**, 4286 (2020).
- [4] D. T. Michel, A. Dolfi-Bouteyre, D. Goular, B. Augère, C. Planchat, D. Fleury, L. Lombard, M. Valla, and C. Besson, Onboard wake vortex localization with a coherent 1.5 μm Doppler lidar for aircraft in formation flight configuration, *Opt. Express* **28**, 14374 (2020).
- [5] L. Liu and R. J. A. M. Stevens, Enhanced wind-farm performance using windbreaks, *Phys. Rev. Fluids* **6**, 074611 (2021).
- [6] T. Chatterjee and Y. T. Peet, Streamwise inhomogeneity of spectra and vertical coherence of turbulent motions in a finite-size wind farm, *Phys. Rev. Fluids* **6**, 114601 (2021).
- [7] M. Jia, J. Yuan, C. Wang, H. Xia, Y. Wu, L. Zhao, T. Wei, J. Wu, L. Wang, S. Y. Gu, L. Liu, D. Lu, R. Chen, X. Xue, and X. Dou, Long-lived high-frequency gravity waves in the atmospheric boundary layer: observations and simulations, *Atmospheric Chem. Phys.* **19**, 15431 (2019).
- [8] Z. Liu, J. F. Barlow, P.-W. Chan, J. C. H. Fung, Y. Li, C. Ren, H. W. L. Mak, and E. Ng, A review of progress and applications of pulsed Doppler wind lidars, *Remote Sensing* **11**, 2522 (2019).
- [9] J. Yuan, K. Wu, T. Wei, L. Wang, Z. Shu, Y. Yang, and H. Xia, Cloud seeding evidenced by coherent Doppler wind lidar, *Remote Sensing* **13**, 3815 (2021).
- [10] V. A. Banakh, I. N. Smalikho, A. V. Falits, and A. M. Sherstobitov, Estimating the parameters of wind turbulence from spectra of radial velocity measured by a pulsed Doppler lidar, *Remote Sensing* **13**, 2071 (2021).
- [11] J. Yuan, Y. Wu, Z. Shu, L. Su, D. Tang, Y. Yang, J. Dong, S. Yu, Z. Zhang, and H. Xia, Real-time synchronous 3-D detection of air pollution and wind using a solo coherent Doppler wind lidar, *Remote Sensing* **14**, 2809 (2022).
- [12] C. F. Abari, A. T. Pedersen, E. Dellwik, and J. Mann, Performance evaluation of an all-fiber image-reject homodyne coherent Doppler wind lidar, *Atmos. Meas. Tech.* **8**, 4145 (2015).
- [13] M. F. van Dooren, A. P. Kidambi Sekar, L. Neuhaus, T. Mikkelsen, M. Hölling, and M. Kühn, Modelling the spectral shape of continuous-wave lidar measurements in a turbulent wind tunnel, *Atmos. Meas. Tech.* **15**, 1355 (2022).
- [14] C. Liang, C. Wang, X. Xue, X. Dou, and T. Chen, Meter-scale and sub-second-resolution coherent Doppler wind lidar and hyperfine wind observation, *Opt. Lett.* **47**, 3179 (2022).
- [15] Y. Wu, Y. Zhang, J. Yuan, Z. Shu, J. Dong, M. Li, L. Zhao, and H. Xia, Suppression of crosstalk in coding cdwl by active fov modulation with a deformable mirror, *Opt. Express* **30**, 29485 (2022).
- [16] Y. Zhang, Y. Wu, and H. Xia, Spatial resolution enhancement of coherent Doppler wind lidar using differential correlation pair technique, *Opt. Lett.* **46**, 5550 (2021).
- [17] Y. Zhang, Y. Wu, and H. Xia, High resolution coherent Doppler wind lidar incorporating phase-shift keying, *J. Lightwave Technol.* **40**, 7471 (2022).
- [18] Y. Zhang, Y. Wu, and H. Xia, Spatial resolution enhancement of coherent Doppler lidar by pseudo-random phase coding, *J. Lightwave Technol.* **40**, 4467 (2022).
- [19] Y. Zhang, Y. Wu, J. Dong, and H. Xia, 1.8 m/0.5 s resolution coherent Doppler wind lidar using continuous phase modulation, *IEEE Photon. J.* **14**, 6047706 (2022).
- [20] S. W. Henderson, P. Gatt, D. Rees, and R. M. Huffaker, Wind lidar, in *Laser Remote Sensing*, edited by T. Fuji and T. Fukuchi (CRC, Boca Raton, FL, USA, 2005), Sec. 7, pp. 520–570.
- [21] M. Liu, Y. Yang, H. Shen, J. Zhang, X. Zou, H. Wang, L. Yuan, Y. You, G. Bai, B. He, and J. Zhou, 1.27 kw, 2.2 Ghz pseudo-random binary sequence phase modulated fiber amplifier with Brillouin gain-spectrum overlap, *Sci. Rep.* **10**, 629 (2020).
- [22] A. Kobayakov, M. Sauer, and D. Chowdhury, Stimulated Brillouin scattering in optical fibers, *Adv. Opt. Photon.* **2**, 1 (2010).
- [23] S. W. Henderson, P. Gatt, D. Rees, and R. M. Huffaker, Wind lidar, in *Laser Remote Sensing*, edited by T. Fuji and T. Fukuchi (CRC, Boca Raton, FL, USA, 2005), Sec. 7, p. 517.

- [24] J. Yuan, H. Xia, T. Wei, L. Wang, B. Yue, and Y. Wu, Identifying cloud, precipitation, windshear, and turbulence by deep analysis of the power spectrum of coherent Doppler wind lidar, [Opt. Express](#) **28**, 37406 (2020).
- [25] B. J. Rye and R. M. Hardesty, Discrete spectral peak estimation in incoherent backscatter heterodyne lidar. I. Spectral accumulation and the cramer-rao lower bound, [IEEE Trans. on Geosci. Remote Sens.](#) **31**, 16 (1993).
- [26] K. R. Sreenivasan, On the universality of the Kolmogorov constant, [Phys. Fluids](#) **7**, 2778 (1995).
- [27] O. Kliebis and P. Mahnke, Real-time laser Doppler anemometry for optical air data applications in low aerosol environments, [Rev. Sci. Instrum.](#) **91**, 095106 (2020).